

REPORT DOCUMENTATION PAGE

AFRL-SR-AR-TR-05-

0507

The public reporting burden for this collection of information is estimated to average 1 hour per response, including the time for reviewing the data needed, and completing and reviewing the collection of information. Send comments regarding this burden estimate or any other aspect of this collection of information, including suggestions for reducing the burden, to Department of Defense, Washington Headquarters Services, Directorate for Information Operations and Reports, 1215 Jefferson Davis Highway, Suite 1204, Arlington, VA 22202-4302. Respondents should be aware that notwithstanding any other requirements that may apply to a collection of information if it does not display a currently valid OMB control number.

PLEASE DO NOT RETURN YOUR FORM TO THE ABOVE ADDRESS.

1. REPORT DATE (DD-MM-YYYY) 19092005		2. REPORT TYPE Final Report		3. DATES COVERED (From - To) 15 Jan 2001 - 30 Apr 2005	
4. TITLE AND SUBTITLE Local Strain Development and Property Variability in B2 Intermetallics				5a. CONTRACT NUMBER	
				5b. GRANT NUMBER F49620-01-1-0159	
				5c. PROGRAM ELEMENT NUMBER	
6. AUTHOR(S) Professor Tresa M. Pollock				5d. PROJECT NUMBER	
				5e. TASK NUMBER	
				5f. WORK UNIT NUMBER	
7. PERFORMING ORGANIZATION NAME(S) AND ADDRESS(ES) Department of Materials Science and Engineering University of Michigan Ann Arbor MI 48109				8. PERFORMING ORGANIZATION REPORT NUMBER	
9. SPONSORING/MONITORING AGENCY NAME(S) AND ADDRESS(ES) USAF/AFRL AFOSR 875 North Randolph Street Arlington VA 22203				10. SPONSOR/MONITOR'S ACRONYM(S) AFOSR	
				11. SPONSOR/MONITOR'S REPORT NUMBER(S)	
12. DISTRIBUTION/AVAILABILITY STATEMENT Distribution Statement A. Approved for public release; distribution is unlimited.					
13. SUPPLEMENTARY NOTES					
14. ABSTRACT The overall objective of this research program was to develop a quantitative understanding of the relationship of straining processes at the scale of microstructure to macroscopic mechanical properties of structural materials. To accomplish this, experimental high-resolution displacement mapping techniques for analysis of strains at the micron scale were developed and validated. Strain accumulation and its relationship to microstructural features in several variants of the B2 intermetallic RuAl were investigated. Significant heterogeneity of straining was observed within individual grains and among neighboring grains in all materials studied. The scale of strain heterogeneity was influenced by grain size and the presence of second phases along grain boundaries. Grain to grain strain distributions developed early in the straining process and strain maps revealed self-similar straining patterns during progressive loading. The relationship between grain-scale strains and deformation mechanisms was studied via dislocation substructure analysis with "targeted" removal of TEM foils with a focused ion beam system. The strain mapping tool proved useful for the identification of active slip systems in the intermetallic RuAl system. Finally, high resolution					
15. SUBJECT TERMS					
16. SECURITY CLASSIFICATION OF:			17. LIMITATION OF ABSTRACT UU	18. NUMBER OF PAGES 24	19a. NAME OF RESPONSIBLE PERSON
a. REPORT U	b. ABSTRACT U	c. THIS PAGE U			19b. TELEPHONE NUMBER (Include area code)

LOCAL STRAIN DEVELOPMENT AND PROPERTY VARIABILITY IN B2 INTERMETALLICS

Final Report
September 19, 2005

AFOSR GRANT NUMBER F49620-01-1-0159

Submitted by:

Co-Principal Investigators:

Professor Tresa M. Pollock
Department of Materials Science and Engineering
University of Michigan, Ann Arbor, MI

and

Professor Marc De Graef
Department of Materials Science and Engineering
Carnegie Mellon University, Pittsburgh, PA

DISTRIBUTION STATEMENT A
Approved for Public Release
Distribution Unlimited

20051215 158

LOCAL STRAIN DEVELOPMENT AND PROPERTY VARIABILITY IN B2 INTERMETALLICS

Table of Contents

Section	Page
1.0 Abstract.....	3
2.0 Research Motivation	4
3.0 The Strain Mapping Technique.....	4
4.0 Intermetallic Aluminides and Selection of Materials System.....	6
5.0 Experimental Materials and Procedures.....	8
6.0 Results.....	10
6.1 Single Phase RuAl Strain Maps.....	10
6.2 Schmid factor analysis.....	12
6.3 FIB-assisted dislocation substructure analyses.....	15
6.4 Strain Maps for Two Phase Materials.....	17
6.5 Strain Gradients and Geometrically Necessary Dislocations.....	19
7.0 Implications of Research.....	20
8.0 References.....	23
9.0 Personnel Supported.....	24
10.0 Publications.....	24

LOCAL STRAIN DEVELOPMENT AND PROPERTY VARIABILITY IN B2 INTERMETALLICS

AFOSR GRANT NUMBER F49620-01-1-0159

Co-Principal Investigators:

Tresa M. Pollock
Department of Materials Science and Engineering
University of Michigan, Ann Arbor, MI

Marc De Graef
Department of Materials Science and Engineering
Carnegie Mellon University, Pittsburgh, PA

1.0 Abstract

The overall objective of this research program was to develop a quantitative understanding of the relationship of straining processes at the scale of microstructure to macroscopic mechanical properties of structural materials. To accomplish this, experimental high-resolution displacement mapping techniques for analysis of strains at the micron scale were developed and validated. Strain accumulation and its relationship to microstructural features in several variants of the B2 intermetallic RuAl were investigated. Significant heterogeneity of straining was observed within individual grains and among neighboring grains in all materials studied. The scale of strain heterogeneity was influenced by grain size and the presence of second phases along grain boundaries. Grain to grain strain distributions developed early in the straining process and strain maps revealed self-similar straining patterns during progressive loading. The relationship between grain-scale strains and deformation mechanisms was studied via dislocation substructure analysis with "targeted" removal of TEM foils with a focused ion beam system. The strain mapping tool proved useful for the identification of active slip systems in the intermetallic RuAl system. Finally,

high resolution EBSD analysis of lattice orientations in samples with strong gradients within strain maps demonstrated that these gradients could not be attributed to the presence of geometrically necessary dislocations.

2.0 Research Motivation

In recent years the need for accelerated characterization and improved prediction of the properties of structural materials has become critical. Designs that utilize new structural materials require knowledge of not only “average” properties, but more importantly, “minimum” properties. While prediction of average properties (such as tensile, fatigue, creep) is challenging, predicting variability in these properties is an even greater challenge. This requires explicit consideration of microstructure and the associated heterogeneity of the plastic straining processes. The overall objective of this research program was to develop a quantitative relationship between microstructure, local straining and macroscopic mechanical response. To accomplish this, experimental high-resolution displacement mapping techniques for analysis of strains at the scale of microstructural features have been developed. Polycrystalline intermetallics were examined by this technique experimentally. Of specific interest was the homogeneity of straining on a grain-to-grain basis, the relationship of straining patterns to grain orientations and strain gradients in the vicinity of grain boundaries.

3.0 The Strain Mapping Technique

The strain mapping technique involves a simple gridding process prior to straining and permits the calculation of strains over large sample areas. The technique is higher in

resolution than many similar techniques that have been developed in the past due to the use of pattern recognition algorithms and gray scales within the acquired images. By utilizing the gray scale information within the back-scattered SEM images, along with image processing algorithms, fine scale in-plane displacement fields of the investigated areas can be extracted through the calculation of individual marker shifts following deformation. Strain fields are calculated using second-order polynomial mapping of the displacements. In this manner, the in-plane strain components (e.g. ϵ_x , ϵ_y and ϵ_{xy} , where the out of plane direction is “z”) can be measured with high precision. A strain resolution of 0.1% is possible with the use of this technique. Since the out of plane displacements are not captured by this technique, the Von Mises effective strains used throughout the paper are defined as:

$$\epsilon_{\text{eff}} = \{ 2[\epsilon_x^2 + \epsilon_y^2 + (\epsilon_x - \epsilon_y)^2 + 6\epsilon_{xy}^2]/9 \}^{1/2} \quad (1)$$

with all the out of plane strain components assumed to be equal to zero, i.e.

$$\epsilon_z = \epsilon_{zy} = \epsilon_{zx} = 0$$

The program has been developed with the use of the Interactive Data Language (IDL). The algorithm requires minimal human intervention, and is capable of dealing with missing data points and large deformations without special accommodations. The technique has been validated by averaging strains measured over large surface areas during step loading and comparing them to the results of conventional macroscopic tensile tests. The technique can be utilized for analysis of *in-situ* straining experiments within the scanning electron microscope or *ex-situ* analysis of strains accumulating during testing by conventional laboratory techniques.

Procedures have been developed for gridding, straining in an Instron (or fatigue apparatus) and analyzing the samples after deformation. While a variety of imaging approaches have been investigated, we have determined that the most effective approach for this type of strain mapping is to utilize the SEM for imaging the grid before and after deformation. This approach permits comparable imaging conditions (with no complications regarding changes in the gray scale due to plasticity-induced surface roughening). Sample alignment in the microscope before and after deformation is an important issue. Accordingly an alignment fixture has been designed for the SEM and image rotations associated with sample re-loading have been minimized.

4.0 Intermetallic Aluminides and Selection of Materials System

Intermetallic B2 aluminides have been the subject of a wide range of microstructure, processing and deformation studies [1-5]. However, most high temperature B2 intermetallics exhibit brittle behavior that significantly hinders their application in bulk form in high temperature structural components. Deformation and transmission electron microscopy studies on B2 aluminides reveal a spectrum of slip behaviors with $\langle 100 \rangle$, $\langle 110 \rangle$ and/or $\langle 111 \rangle$ dislocation gliding, depending on alloy composition and deformation temperature [4]. At ambient temperature, the plastic behavior of low melting point compounds is distinctively different from high melting point temperature compounds. Slip in low temperature compounds such as FeAl occurs primarily by glide of $\langle 111 \rangle$ dislocations on $\{110\}$ planes. Whereas in high temperature compounds such as NiAl, deformation is controlled by motion of $\langle 100 \rangle$ dislocations on $\{100\}$ and $\{110\}$ planes [1, 4]. At the same time, dislocation mobility is also limited in many high temperature B2 intermetallics [6]. Brittleness arises due

to lack of dislocation mobility and/or insufficient number of independent slip systems to satisfy the Von Mises criterion [7]. NiAl is an example of the high temperature B2 aluminides without sufficient dislocation mobility or enough slip systems [3]. In this case, polycrystalline NiAl fail in a brittle manner at low strains.

The intermetallic RuAl, with a melting temperature of 2068°C, displays a very unusual plastic behavior compared to other types of high temperature B2 intermetallics. It exhibits both unusually high room temperature “chisel toughness” [8] and diverse deformation characteristics [6, 9-13]. From an applications point of view, this B2 intermetallic is of interest as a bond coat material for thermal barrier coating systems that are utilized to extend the temperature capabilities of nickel-base single crystal superalloys.

In binary RuAl, deformation occurs on $\langle 100 \rangle \{110\}$ & $\langle 110 \rangle \{110\}$ slip systems [10]. Whereas in RuAl based ternary systems with additions of either Pt or Ta, dislocation glide occurs primarily on the $\langle 111 \rangle \{110\}$ system [11-13]. Slip on either a combination of $\langle 100 \rangle \{110\}$ and $\langle 110 \rangle \{110\}$ systems (binary RuAl) or $\langle 111 \rangle \{110\}$ systems (ternary RuAl) can provide sufficient modes of deformation for compatible straining of polycrystalline. Accompanying the ample number of slip systems is the high apparent dislocation mobility in RuAl compound [6, 12, 13].

Given the diversity of slip systems in RuAl, the aim of this research was to examine the plastic behavior of this compound in greater detail with emphasis on developing a quantitative understanding of the relationship of the straining process at the scale of the

microstructure and its macroscopic mechanical properties. Several different variants of single phase and two phase RuAl have been investigated. Two phase materials were composed of RuAl grains with δ -Ru along the grain boundaries.

5.0 Experimental Materials and Procedures

Three different compositions of near-stoichiometric RuAl alloys were investigated. These included 52Ru48Al (with excessive δ -Ru along grain boundaries), 48Ru50Al2Nb-0.5B (limited δ -Ru) and 48Ru52Al (no δ -Ru). Alloys were fabricated by levitation melting in a MCGS5 Crystalox system equipped with a copper cold crucible. Following melting, a homogenization heat treatment at 1350°C for 36 hours in Ar-filled SiO₂ capsule was conducted. Sample for compression testing was sectioned from the melt button by electro discharge machining (EDM) to a final dimension of 5mm x 5mm x 10mm. The surface selected for surface displacement mapping of the sample was then mechanically polished down to 0.05 μ m Al₂O₃ finish before electropolishing in an electrolyte of 10% lactic acid, 7% sulfuric acid, 3% nitric acid, 2% hydrofluoric and methanol in the temperature range of -30~40°C, at 20~25 volts [15]. EBSD experiment was conducted for the as-polished, undeformed sample in a Philips XL30 field emission gun SEM equipped with TSL OIM[®] module. The step size for the EBSD scan was 3 μ m.

During surface displacement mapping, a 2000 lines/inch commercially available nickel mesh grid (corresponding to c.a. 6 μ m x 6 μ m marker size) was used to deposit gold markers on the as-polished surface. Surface displacement mapping tests were carried out by means of ex-situ stepped loading compression tests, where the sample was taken to image in SEM between loading intervals. A total of four loading steps were applied and the nominal cumulative

compressive strain after each step was 1.50%, 2.07%, 3.14% and 3.65%, respectively. All the tests were conducted at a strain rate of the order 10^{-4} /s by utilizing a compression fixture in an Instron model 5582 screw driven machine. The displacement between platens of the compression fixture was measured by a pair of linear variable capacitance transducers. Displacement mapping and subsequent strain calculation were conducted with the IDL-based strain mapping algorithms developed for this research program.

Following displacement mapping, a series of thin foils used for TEM dislocation analysis were sectioned from the interior of representative grains that underwent different degrees of deformation, as determined by displacement mapping. The foils preparation was conducted with the use of a focused ion beam (FIB) in a FEI Nova Nanolab dual beam system. A slightly modified version of the standard “cross-section” and “lift-out” techniques [16] were used for preparation of these foils. Additional polishing of the as-FIBed foils were carried out in a Gatan 691 Precision Ion Milling System (PIPSTM) for reduction of surface damage induced by the high energy gallium ions in the dual beam system. Typical resultant foil size was about $15\mu\text{m} \times 5\mu\text{m} \times 0.1\mu\text{m}$. TEM analyses were conducted in a Philips CM-12 microscope with a double tilt holder. Seven to ten different diffraction vectors (\mathbf{g}) were used to determine the Burgers vector of dislocations.

6.0 Results

6.1 Single Phase RuAl Strain Maps

The initial microstructure of 48Ru52Al with markers deposited on surface is shown in Fig. 1. Grain boundaries were artificially highlighted for easy recognition. Grain sizes in the post heat treated materials were typically in the range of 200~400 μm .

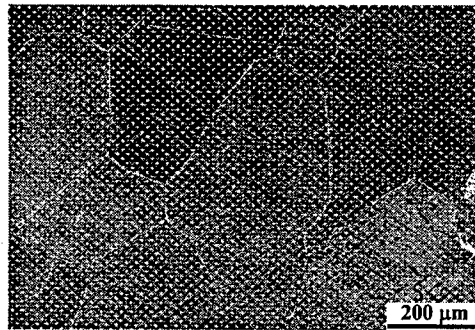


Fig. 1 Initial microstructure of 48Ru52Al. Arrays of white dots are gold markers deposited on the surface.

Fig. 2(a)~2(d) shows the Von Mises effective strain maps calculated after each of the 4 stepped loading compression tests of the same cluster of grains. The microstructure with markers on surface was overlaid with the maps. All the strain maps are plotted under the same color scale running from a minimum 0.08% to a maximum 9.85% of strain. The external loading axis was along “y” direction. The statistics of the effective strain maps are summarized in Table 1.

Examination of strain maps reveals significant strain heterogeneity developing early in the straining process, with a strong local microstructural influence. Individual grains, for

example grains "A", "B" and "C" (marked in Fig. 2(a)), accumulated different amounts of strain after each step of deformation. Grain "A" deformed most favorably over all its neighboring grains, accumulating the highest strains at an early stage of deformation, and continuing to be the most heavily deformed grain throughout the tests. Grain "B" experienced a lower degree of straining compared to grain "A". The strains within grain "B" gradually built up as the overall imposed strain increased. At the end of step 4, it accumulated the second highest strain among the grains within the field of view. Grain "C" was the least favorably prone to deformation, with very low strain levels even after the majority of its neighboring grains underwent rather large degree of deformation. The highest strains appear at a grain boundary triple point during all four stages of deformation, apparently due to the excessive geometric constraints that built up stress locally. As the nominal strain increased following each loading step, the highest strain gradually evolved into a narrow band of approximately 20 μ m wide along the grain boundary on the high-strain-grain (grain "A") side. Several other high strain regions were observed near grain boundaries within the same grain. A close comparison of the four effective strain maps in Fig. 2 indicates that the pattern of strain heterogeneity that developed at the very early stage of deformation persisted to the higher strain levels.

According to strain maps statistics, Table 1, the maximum strain found in the effective strain map within each step was approximately 3X of the average value of the entire map, while the minimum strain was almost an order of magnitude lower than the average.

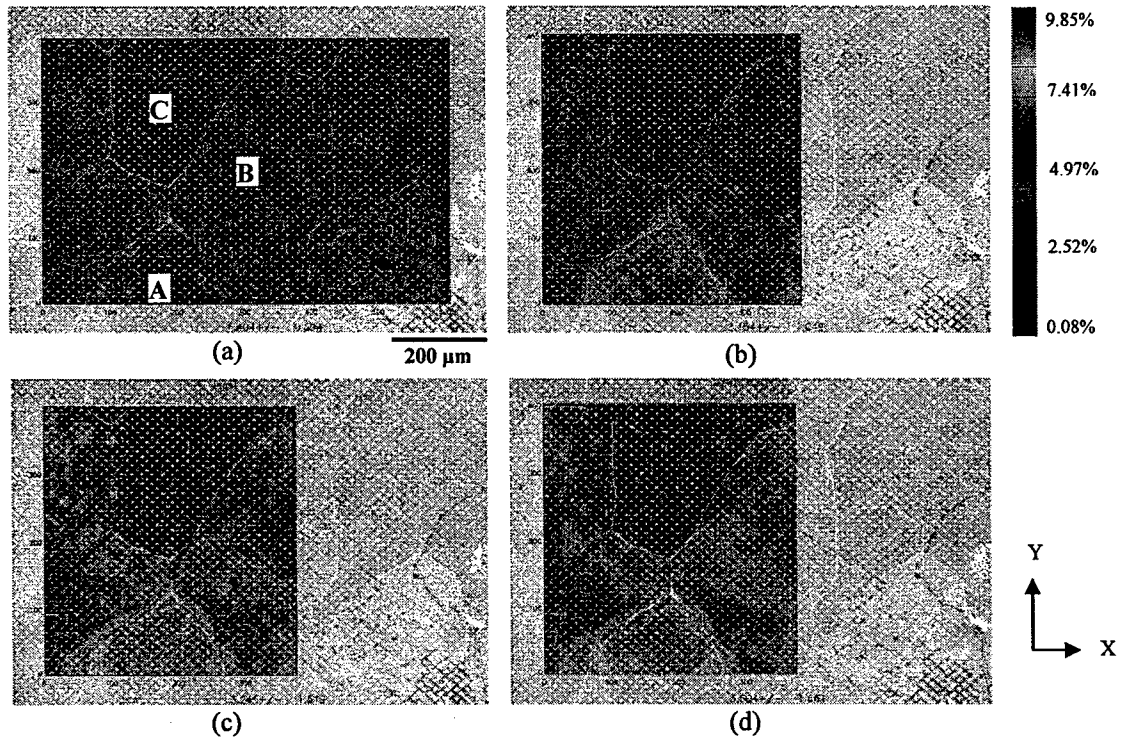


Fig. 2 Effective strain maps of 48Ru52Al after nominal compression of (a) 1.50%, (b) 2.07%, (c) 3.14%, and (d) 3.65% strain

Table 1. Statistics of effective strain maps of 48Ru52Al

	Nominal imposed strain	Avg. strain in the map	Std. dev. of Avg. strains	Max. strain in the map	Max. /Avg. ratio	Min. strain in the map	Min./Avg. ratio
Step 1	1.50%	1.40%	0.59%	4.49%	3.21	0.08%	0.06
Step 2	2.07%	2.15%	1.05%	6.45%	3.00	0.27%	0.13
Step 3	3.14%	3.25%	1.52%	9.47%	2.91	0.34%	0.10
Step 4	3.65%	3.50%	1.66%	9.85%	2.81	0.54%	0.15

6.2 Schmid factor analysis

Grain orientations of the cluster of grains being investigated here were acquired by EBSD before sample deformation. Results are shown in Fig. 3(a). Note that the map only presents orientations that are along the out of plane direction. The in-plane orientations are not shown by the map but are readily extracted from the EBSD scan data. With the input of point-wise orientation data and considering the loading direction (along “y”), it is possible to evaluate the contributions of individual slip systems during straining by calculating their respective Schmid factors among these grains. A Matlab program was used to conduct the calculation and the results are shown in Fig. 3(b)~3(d). Note that all the Schmid factor plots are drawn under the same color scale (from 0.024~0.490). Fig. 3(b) is a composite Schmid factor plot, which adopted maximum calculated Schmid factor between the two slip systems at each data point. Fig. 3(c)~3(d) are the Schmid factor plots for individual $\langle 100 \rangle \{110\}$ and $\langle 110 \rangle \{110\}$ slip systems.

Considering the composite Schmid plot in Fig. 3(b), there is only a minor variation in Schmid factor from grain to grain. For example, grain “A” has essentially the same Schmid factor as grain “C”. This suggests that if both slip systems were equally favorably activated during deformation, there would be no preference for excessive straining between these two individual grains. However, this is not true, as was demonstrated by the effective strain maps that there existed significant difference in the strain concentration between grain “A” and grain “C”. On the other hand, Schmid plots for the individual slip system show substantial differences in Schmid factor among neighboring grains. In $\langle 100 \rangle \{110\}$ Schmid plot,

Fig 3(c), grain “A” has the smallest Schmid factor, followed by grain “B” with a intermediate Schmid factor and grain “C” with the largest among the three. In the $\langle 110 \rangle \{110\}$ Schmid plot, Fig. 3(d), exactly the opposite is observed. Comparing to the amount of strain developed within these grains, Fig. 1(d), there exists a close correlation between large $\langle 110 \rangle \{110\}$ Schmid factors and high strain concentration among these grains. This indicates that the $\langle 110 \rangle \{110\}$ slip system may be favored within the grains analyzed in the experiments.

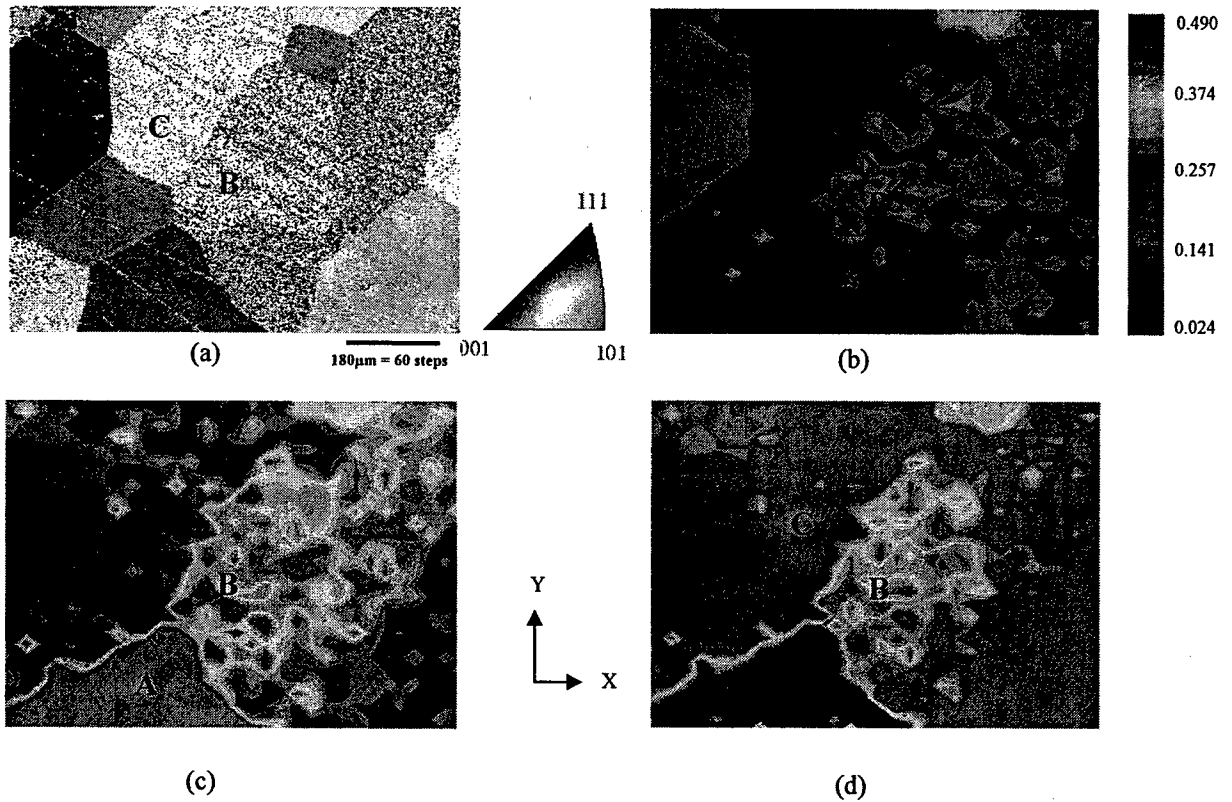


Fig. 3 (a) Grain orientation map of 48Ru52Al alloy obtained by EBSD, (b) Composite Schmid factor plot for the maximum of $\langle 100 \rangle \{110\}$ or $\langle 110 \rangle \{110\}$ slip, (c) Schmid factor plot for $\langle 100 \rangle \{110\}$ slip system, (d) Schmid factor plot for $\langle 110 \rangle \{110\}$ slip system

6.3 FIB-assisted dislocation substructure analyses

Fig. 4(a)~4(f) shows a series of dislocation bright field images taken under different diffraction conditions from the foil cut from the most heavily strained grain "A". Some randomly distributed dark spots can be seen in the backgrounds of the images. These are direct results of foil surface damage which had not been completely removed during final polishing in PIPS.

The area shown is characterized by the presence of high density of tangled dislocations. Such characteristic substructure was also observed in other regions of the foil. This is consistent with the high strain concentration in the grain. Dislocations near the center of the images have been identified as having Burgers vector of with $g = [\bar{1}\bar{1}0]$, given their invisible conditions at $g = [\bar{1}\bar{1}0]$ and $g = [\bar{1}\bar{1}1]$. Another set of $\langle 110 \rangle$ type dislocations are also identified near the lower left corner of the images. Significant density reduction at $g = [\bar{1}00]$ and $g = [0\bar{1}1]$ in this region as compared to $g = [\bar{1}01]$ suggest that the majority of the dislocations have a $[011]$ Burgers vector. The presence of $\langle 100 \rangle$ type dislocations is less frequently observed. One example is a short segment near the middle left side of the images that identified as having a $[010]$ Burgers vector and becomes invisible at $g = [\bar{1}00]$ and $g = [\bar{1}01]$. Clearly, the density of $\langle 110 \rangle$ type dislocations is significantly higher than that of $\langle 100 \rangle$ type. In addition, a small number of $[111]$ dislocations are also observed near the upper right side of the images with invisible conditions at $g = [110]$ and $g = [011]$.

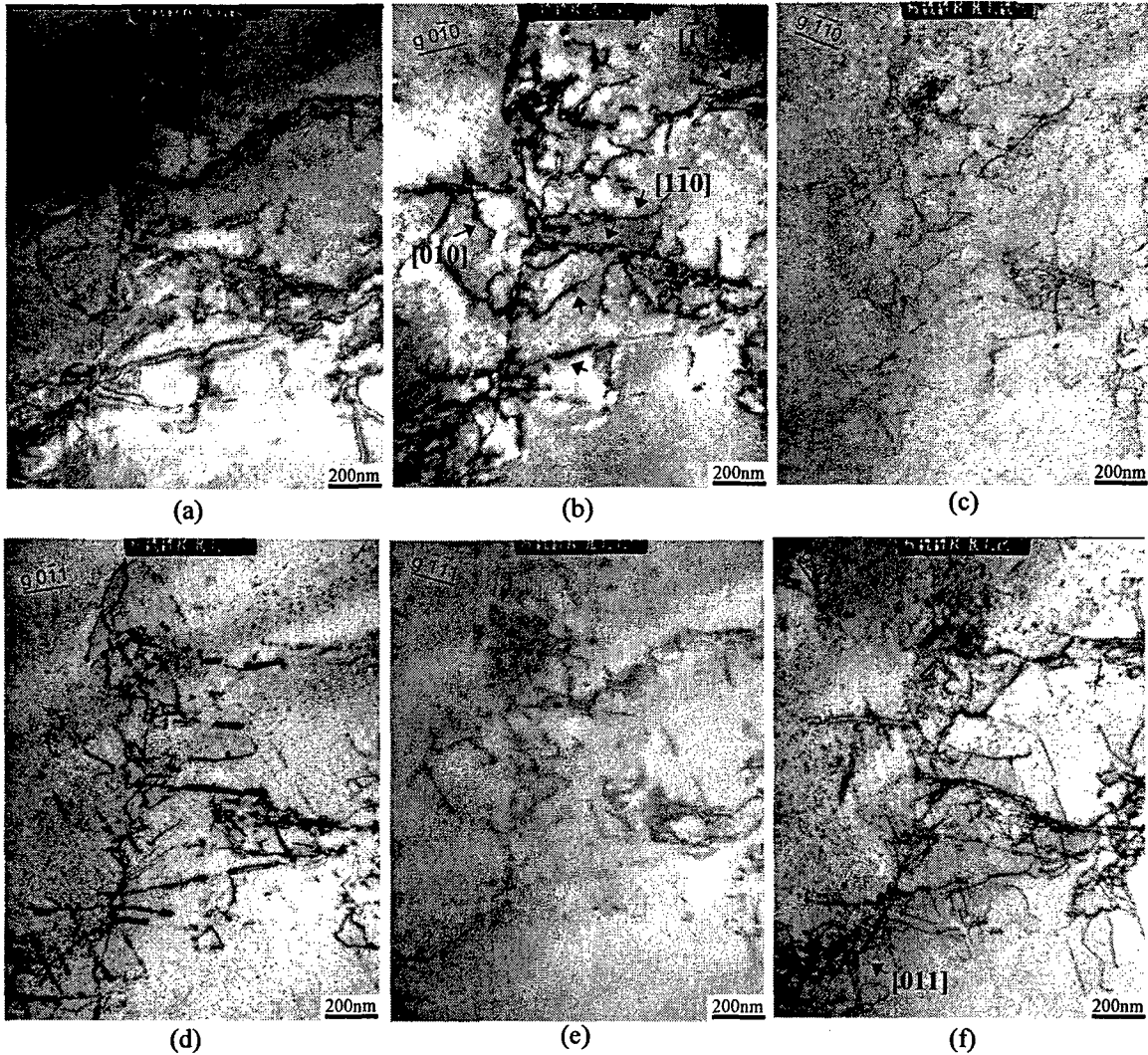


Fig. 4 Bright field images of dislocations observed in FIBed TEM foil from the most heavily strained grain "A". Dislocations of $\langle 110 \rangle$, $\langle 100 \rangle$ and $\langle 111 \rangle$ type Burgers vector are found. The majority of dislocations are identified as having Burgers vector of $\langle 110 \rangle$ type.

Fig. 5(a)~5(f) shows a series of dislocation bright field images taken under different diffraction conditions from the foil cut from the least strained grain "C". The dislocation density within the foils cut from this grain is indeed very low. The area shown in Fig. 5(a)~5(f) represents one of the few regions within the foil that contained a significant density of dislocations. Dislocations within this region can be characterized by the presence of several long segments, a few dipole loops and aggregates of very short entangled segments.

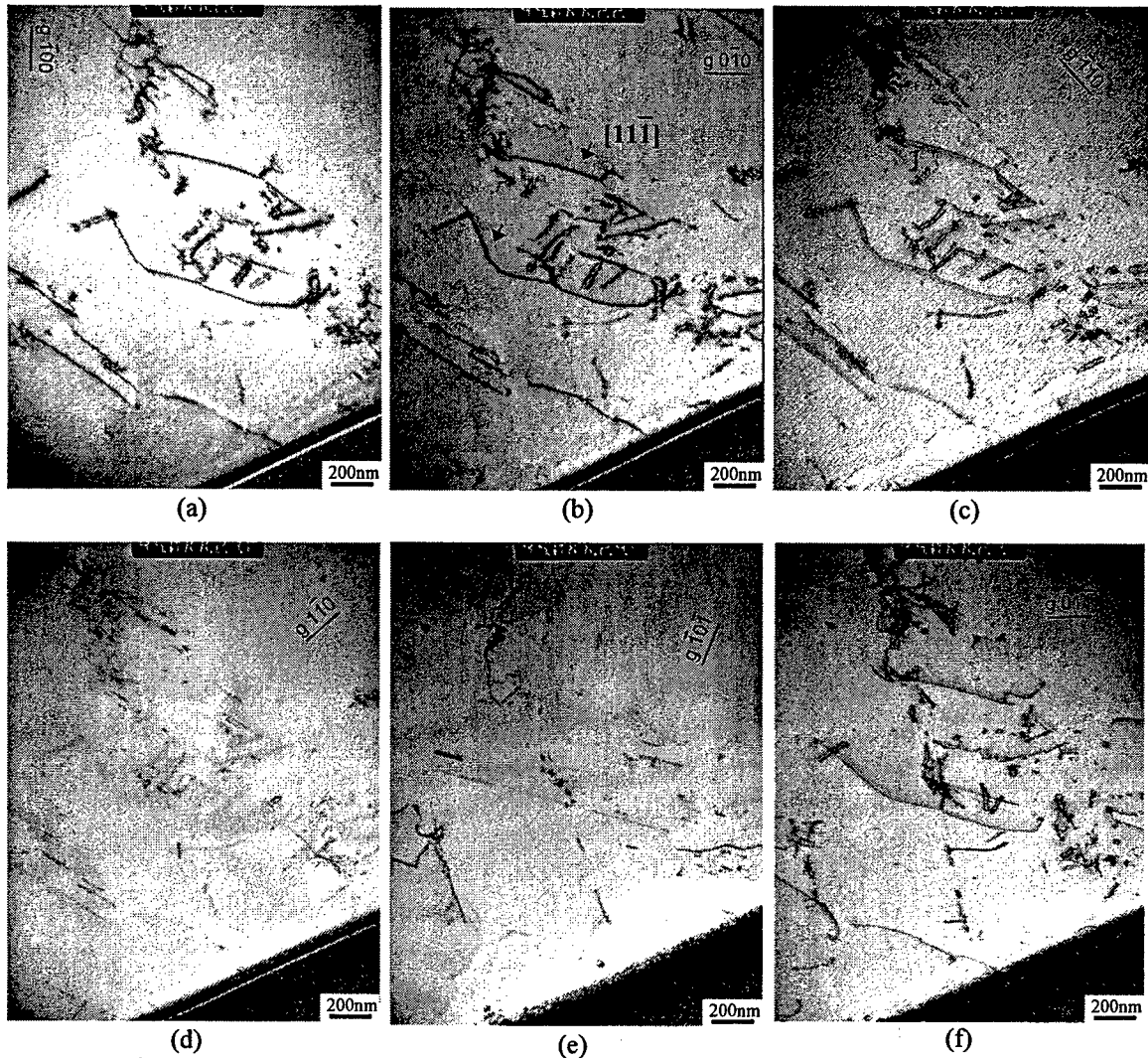


Fig. 5 Bright field images of dislocations observed in FIBed TEM foil from the least strained grain "C". The majority of dislocations are identified as having $\langle 111 \rangle$ type Burgers vector.

A majority of dislocations become invisible with $g = [1\bar{1}0]$ and $g = [\bar{1}0\bar{1}]$, indicating that their Burgers vectors are of $[11\bar{1}]$ type. However, since $\langle 111 \rangle$ slip is not the major type of active slip identified in this material [10], and given the very low strain concentration within this grain, it is likely that these $\langle 111 \rangle$ type dislocations did not result from dislocation motion but rather remains as a result of the high temperature processing of the original material. The

presence of $\langle 111 \rangle$ dislocations following processing of this compound has also been previously observed [17].

6.4 Strain Maps for Two Phase Materials

The two phase materials included 52Ru48Al (with excessive δ -Ru along grain boundaries) and 48Ru50Al2Nb-0.5B (limited δ -Ru). Fig. 6 shows microstructures and corresponding strain maps after compression to several percent strain. The compression loading axis is along the vertical direction in all cases.

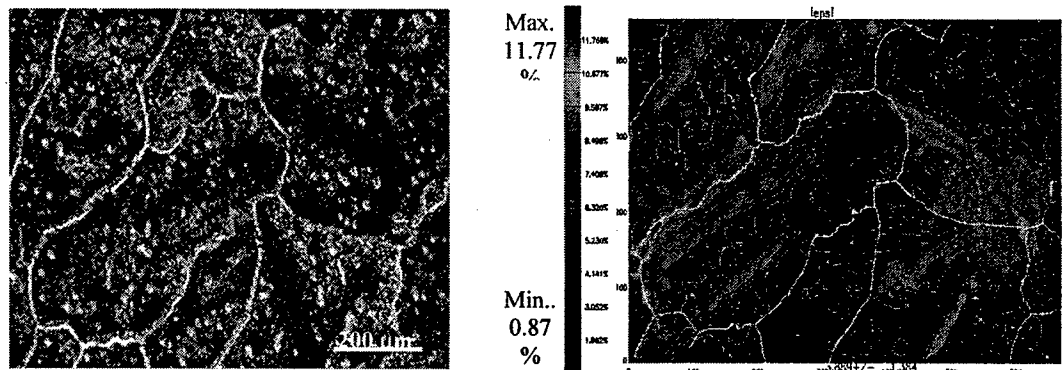


Fig. 6(a) 52Ru48Al consisting of RuAl with excess δ -Ru at grain boundaries and as occasional precipitates in grain interiors. A corresponding 2-D (assuming $\epsilon_z=0$) Von Mises effective strain map after 4.0% nominal compression. Grain boundaries are intentionally delineated in the map.

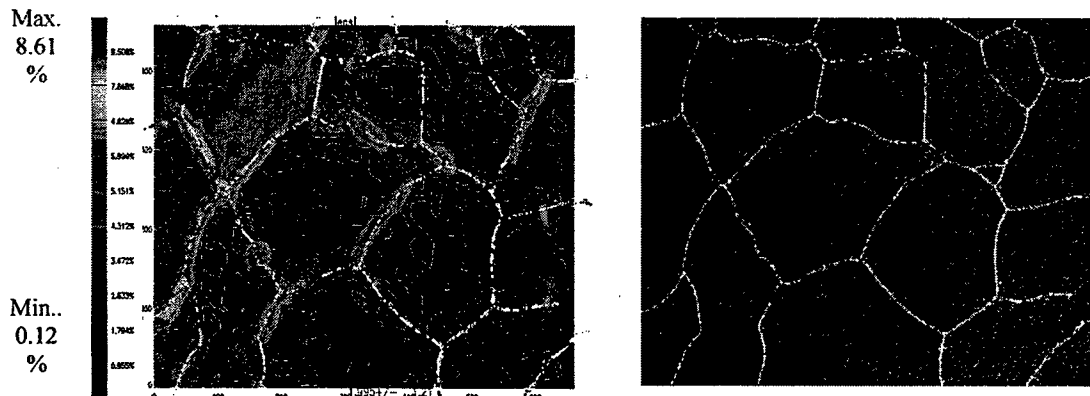
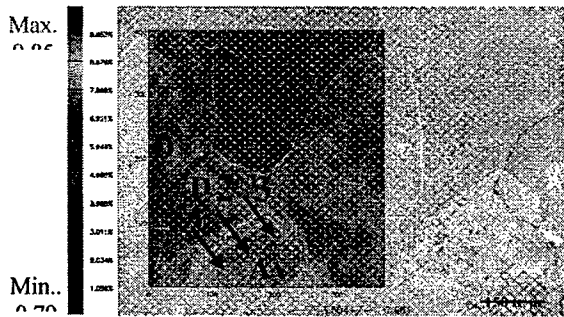


Fig. 6(b) Microstructure of 48Ru50Al2Nb-0.5B. Limited δ -Ru phase (bright contrast) exists only along grain boundaries. Also a 2-D Von Mises effective strain map after 1.6% nominal compression. Grain boundaries are intentionally delineated in the map.

It is interesting to note that there is a tendency for strain to accumulate in the vicinity of the grain boundaries where the δ -Ru phase is present, Figures 6(a) and (b). This phase is located along the boundaries as a result of the final eutectic solidification process and is reported to improve compressional ductility by acting as a “compliant” layer [21]. The results obtained here support this hypothesis. Nanoindentation experiments conducted on the grain boundary δ -Ru before and after plastic straining (at a boundary that experienced enhanced straining) reveal a significantly higher degree of hardening of the δ -Ru, compared to the adjacent RuAl material.

6.5 Strain Gradients and Geometrically Necessary Dislocations

Finally, it is interesting to consider whether the enhanced strains that accumulate along the boundaries are in any way related to geometrically necessary dislocations [22, 23]. High resolution EBSD measurements of local lattice orientation were conducted along the 3 reference lines indicated in Figure 7. Using the theory of Nye [23], geometrically necessary dislocation densities were calculated, considering both $\{110\}\langle 100\rangle$ and $\{110\}\langle 011\rangle$ systems and using the lower-bound Simplex method of El-Dasher and Rollett. The distribution of GND density is compared to the equivalent (total) strain gradients measured by the strain mapping technique in Figure 7. Interestingly, there is no strong correlation between the GNDs and the strains measured via strain mapping. This suggests that plastic gradients in the vicinity of the boundaries do not develop due to the need for GNDs.



Von Mises effective strain map with grain A & D marked

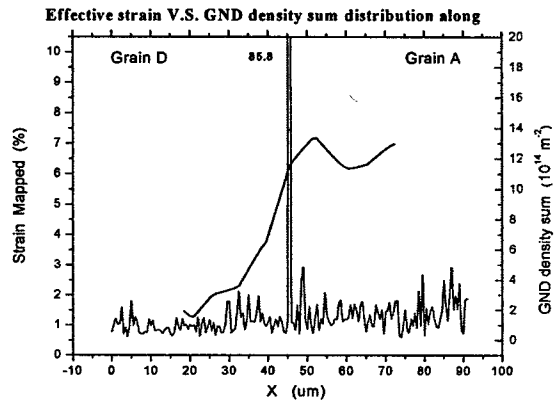
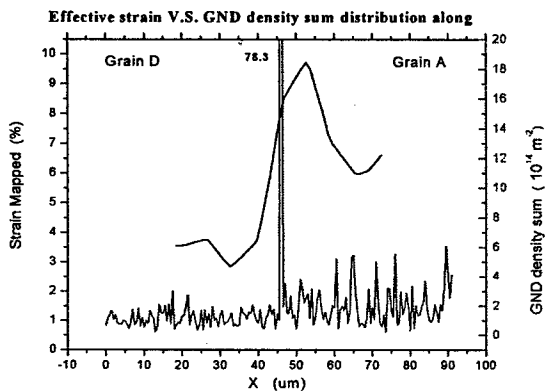
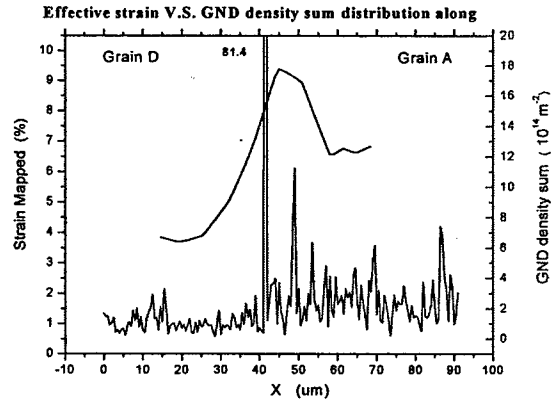


Figure 7 – Distribution of geometrically necessary dislocations (measured via EBSD) compared to Mises equivalent strains (measured by strain mapping). Distributions are along lines marked “1” through “3”. The spike in the GND at the grain boundary is an artifact.

7.0 Implications of Research

The Von Mises effective strain maps of single phase polycrystalline 48Ru52Al after a few percent of nominal compressive deformation show a substantial influence of local microstructure. Considerable strain heterogeneity existed among neighboring grains with strains varying by a factor of 3 (higher) to 10 (lower) from the mean imposed strains. This is interesting given the availability of two different slip systems in this material. That different grains accumulate different amounts of strain indicates that some grains are initially more favorable for deformation. Another distinctive feature of the strain maps is the appearance of

self-similar straining patterns at all four stages of loading. According to crystal plasticity modeling, softer (more favorably) oriented grains will preferentially deform in the early stages of deformation [18]. It is generally believed that when the softer areas harden and become more difficult to deform, further deformation will be mostly concentrated within grains that undergo relatively less amount of deformation during initial straining. Under these conditions, local deformation will not display self-similar strain heterogeneity patterns during different stages of straining. However, the experimental observations shown here suggest that actual deformation behavior is more complicated. It is interesting that such self-similar straining patterns were also observed in TiAl alloys [19]. Given the high strain hardening rates in intermetallics [20], this behavior is somewhat unexpected.

Coupled with strain mapping, the application of EBSD grain orientation analysis and FIB-assisted TEM dislocation investigation provides a unique opportunity to isolate and assess the influence of individual slip systems on the local straining behavior. Prior studies on dislocation substructures in RuAl have typically revealed the presence of both $\langle 100 \rangle$ and $\langle 110 \rangle$ dislocations. Thus it has been unclear which system would be preferred in terms of the ease of activation of the system. To the authors' knowledge, there have not yet been detailed measurements of critical resolved shear stresses on the observed slip systems due to the difficulty of growing single crystals of this high melting point, high Al content compound.

It is not unexpected to see that the results of composite Schmid factor calculation, Fig. 3(b), did not correlate well with the actual strain development profile. For one could anticipate at

least some difference between the $\langle 100 \rangle$ and $\langle 110 \rangle$ slip systems due to the difference in the magnitude of the Burgers vectors. Calculation of dislocation line tensions [17] have indicated a lower energy for $\langle 100 \rangle$ dislocations compared to $\langle 110 \rangle$ dislocations. Thus it is expected that initiation of $\langle 100 \rangle$ slip would be easier than $\langle 110 \rangle$ slip under equal conditions. It is interesting that $\langle 110 \rangle \{110\}$ slip system is dominant within the grains studied here, as confirmed both by the results of Schmid factor analysis and dislocation substructure investigations. The dominant presences of $\langle 110 \rangle$ slip could be influenced by a number of factors, including availability of $\langle 100 \rangle$ vs. $\langle 110 \rangle$ dislocation sources within individual grains, variations of chemistry and defect concentration among neighboring grains, and the specific mechanical constraints imposed on the locally straining grains.

As a corollary, a survey over large number of grains using similar experimental techniques should be able to identify two other possible situations: 1.) highly strained grains dominated by $\langle 100 \rangle$ slip and, 2.) highly strained grains with nearly equal $\langle 100 \rangle$ and $\langle 110 \rangle$ slip. Interestingly, previous dislocation investigation using foils prepared by conventional methods did reveal grains of each of these three types [9, 10]. Nevertheless, the dominant presence of $\langle 110 \rangle$ dislocations observed in this study suggests that the critical resolved shear stress for $\{110\} \langle 110 \rangle$ slip is lower than $\{110\} \langle 100 \rangle$. It is possible that the CRSS is influenced by departures from stoichiometry. Further studies across a range of composition would provide additional information on this chemistry effect. Last but not least, although local geometry constraints almost certainly affect the straining behavior of individual grains, given the strain concentrations in the vicinity of grain boundaries, their impact on the overall straining response is difficult to quantify. Finally, while strain concentrations do often

develop in the vicinity of the grain boundaries, the EBSD measurements demonstrate that these gradients are not due to the presence of a high density of geometrically necessary dislocations.

With regard to two phase materials, the strain mapping procedure is useful for elucidation of the role of the second phase (δ -Ru) in the deformation process. The softer hexagonal phase deforms preferentially, with substantial hardening. Thus the enhanced toughness may indeed arise due to the fact that the second phase serves as a “compliant layer”.

8.0 References

1. Yamaguchi M, Umakoshi Y. Progress in Materials Science 1990;34:1.
2. Miracle DB. Microscopy research and technique 1993;41:649.
3. Noebe RD, Bowman RR, Nathal MV. Int Mater Rev 1993;38:193.
4. Baker I. Materials Science and Engineering A 1995;192-193:1.
5. Nabarro FRN, de Villiers HL, *The Physics of Creep*. 1995, Bristol: Taylor & Francis.
6. Pollock TM, Lu DC, Shi X, Eow K. Materials Science and Engineering A 2001;317:241.
7. Von Mises R. Z. Angew. Math. Meth. 1928;8:161.
8. Fleischer RL, Zabala RJ. Metallurgical Transactions A 1990;21A:2709.
9. Fleischer RL, Field RD, Briant CL. Metallurgical Transactions A 1991;22A:403.
10. Lu DC, Pollock TM. Acta Materialia 1999;47:1035.
11. Nandy TK, Feng Q, Banerjee D, Gigliotti MFX, Pollock TM. in *Defect Properties and Related Phenomena in Intermetallic Alloys* 2003, Warrendale, PA, 2003, p. 89.
12. Nandy TK, Feng Q, Pollock TM. Scripta Materialia 2003;48:1087.
13. Feng Q, Nandy TK, Tryon B, Pollock TM. Intermetallics 2004;12:755.
14. Biery N, De Graef M, Pollock TM. Metallurgical and Materials Transactions A 2003;34A:2301.
15. Somani MC, Muraleedharan K, Birla NC, Singh V, Prasad RVRK. Metall.Mater.Trans.A 1994;25A:1693.
16. Giannuzzi LA, Stevie FA. Micron 1999;30:197.
17. Lu DC, *The dislocation substructures and mechanical properties of RuAl-based intermetallics compounds*, in *Materials Science and Engineering*. 2000, Carnegie Mellon University: Pittsburgh.
18. Asaro RJ. Advances in Applied Mechanics 1983;23:1.
19. Biery N, *Local deformation and bulk properties in Gamma-TiAl based alloys*, in *Materials science and engineering*. 2000, Carnegie Mellon University: Pittsburgh.

20. Cerreta E, Gray GT, Chen SR, Pollock TM. Metallurgical and Materials Transactions A 2004;35A:2557.
21. Wolff I.M. and G. Sauthoff, 1997, Acta Mater. 45, 7, pp. 2949-2969.
22. Ashby M.F., Phil. Mag. 1970, 21, 399.
23. Nye. J.F. Acta Metall.,1953, 153.

9.0 Personnel Supported

Marc De Graef	Professor, Carnegie Mellon University
Qidi Chen	Graduate Student, Carnegie Mellon
Tresa M. Pollock	Professor, University of Michigan
Aomin Wu	Graduate Student, University of Michigan

10.0 Publications

N.E. Biery, M. De Graef and T.M. Pollock, "A Method for Measuring Microstructure Scale Strains: Application to Gamma Titanium Aluminides", Metallurgical and Materials Transactions 34A, 2301, (2003).

G. Chaada, A. Wu., Q. Chen, J.W. Jones, T.M. Pollock and M. De Graef. "In-situ and Ex-situ Surface Displacement Measurements, Proc. Soc. Experimental Mechanics, Charolette, NC, (2003).

A. Wu, T.M. Pollock and M. De Graef, "Development of Strains at the Grain Scale in Near Stoichiometric Polycrystalline RuAl Alloys", to be submitted to Acta Materialia, October 2005.

A. Wu, T.M. Pollock and M. De Graef Grain-scale Strain Mapping for Analysis of Slip Activities in Polycrystalline B2 RuAl, submitted to Phil Mag, Sept. 2005.

A. Wu, B.S. El-Dasher, A.D. Rollet, T.M. Pollock, M. De Graef, "Measurement of geometrically necessary dislocations in inhomogeneously deformed near-grain boundary regions of polycrystalline RuAl", to be submitted to Acta Materialia, October 2005.

A. Wu, J. Madison, T.M. Pollock and M. De Graef, "Grain Size-Induced Straining Inhomogeneities in a Polycrystalline Nickel Base Superalloy", to be submitted to Scripta Mater, November 2005.